JM PAPERS

On the low-frequency flapping motion in flow separation

Xingjun Fang[1],† **and Zhan Wang**[1],†

[1]Key Laboratory for Mechanics in Fluid Solid Coupling Systems, Institute of Mechanics, Chinese Academy of Sciences, Beijing 100190, PR China

Transitional separating flow induced by a rectangular plate subjected to uniform incoming flow at Reynolds number (based on the incoming velocity and half plate height) 2000 is investigated using direct numerical simulation. The objective is to unveil the long-lasting mystery of low-frequency flapping motion (FM) in flow separation. At a fixed streamwise-vertical plane or from the perspective of previous experimental studies using pointwise or planar measurements, FM manifests as a low-frequency periodic switching between low and high velocities covering the entire separation bubble. The results indicate that in three-dimensional space, FM reflects an intricate evolution of streamwise elongated streaky structures under the influence of separated shear layer and mean flow reversal. The FM is an absolute instability, and is initiated through a lift-up mechanism boosted by mean flow deceleration near the crest of the separating streamline. At this particular location, the shear bends the vortex filament abruptly, so that one end is vertically struck into the first half of the separation bubble, whereas the other end is extended in the streamwise direction in the second half of the separation bubble. These two ends of vortex filament are mutually sustained and also stretched by the vertical acceleration and streamwise acceleration in the first and second halves of the separation bubble, respectively. This process periodically switches the low-velocity (or high-velocity) streaky structure to a high-velocity (or low-velocity) streaky structure encompassing the entire separation bubble, and thus flaps the separated shear layer up and down in the vertical direction. A 'large vortex' shedding manifests when the streaky structure switches signs. This large vortex is fundamentally different from the spanwise vortex shedding residing in the shear layer originated from the Kelvin–Helmholtz instability and successive vortex amalgamation. It is also believed that the three-dimensional evolution of streaky structures in the form of FM is applicable for both geometry- and pressure-induced separating flows.

Key words: boundary layer separation

† Email addresses for correspondence: fangxj@imech.ac.cn, zwang@imech.ac.cn

References	St_{Lr} of FM
Eaton & Johnston (1982)	0.15
Kiya & Sasaki (1983)	0.12–0.2
Driver, Seegmiller & Marvin (1987)	0.18
Tafti & Vanka (1991)	0.15
Spazzini *et al.* (2001)	0.08
Hudy, Naguib & Humphreys (2003)	0.11
Cimarelli, Leonforte & De Angeli (2018)	0.15
Chiatto *et al.* (2021)	0.12

Table 1. Strouhal numbers ($St_{Lr} \equiv f L_r / U_\infty$) of FM reported in the literature.

1. Introduction

Separating flow is significant not only for countless environmental and engineering applications, but also for academic understanding of fundamental mechanisms of turbulence. One of the outstanding challenges to a complete understanding of separating flow and its control is the low-frequency flapping motion (FM). To the best knowledge of the authors, the first data that supported a large-scale unsteadiness in flow separation date back nearly half a century ago, and are credited to Fricke (1971), who performed wall-pressure measurement downstream of a surface-mounted fence. This large-scale unsteadiness was later observed in a wide range of configurations of flow separations, including those induced by a backward-facing step (Eaton & Johnston 1982; Driver *et al.* 1987), forward-facing step (Largeau & Moriniere 2007), fence (Hudy *et al.* 2003), Ahmed body (Thacker *et al.* 2013), adverse pressure gradient (Mohammed-Taifour & Weiss 2016), ramp (Chiatto *et al.* 2021) and rectangular plate (Kiya & Sasaki 1983; Cherry, Hillier & Latour 1984; Tafti & Vanka 1991; Cimarelli *et al.* 2018; Fang, Tachie & Dow 2022). As summarized in table 1, in spite of the differences in flow configurations and Reynolds numbers, the frequency f of such a large-scale unsteadiness is, surprisingly, consistent with $f \in [0.08, 0.20] U_\infty / L_r$ (where U_∞ and L_r are the incoming velocity and mean reattachment length, respectively). The structural manifestation of FM, on the other hand, has been investigated using a discrete-vortex model (Kiya, Sasaki & Arie 1982), a pressure–velocity correlation (Kiya & Sasaki 1983; Cherry *et al.* 1984; Tafti & Vanka 1991), smoke (or dye) visualization (Cherry *et al.* 1984; Passaggia, Leweke & Ehrenstein 2012), or a proper orthogonal decomposition (POD) mode (Thacker *et al.* 2013; Mohammed-Taifour & Weiss 2016; Chiatto *et al.* 2021), etc. It is generally accepted that this large-scale unsteadiness features a flapping motion (hence the name) of the shear layer near the separating point, a quasi-periodic sequence of enlargement and shrinkage of the separation bubble, and a 'large vortex' shedding.

Over the past four decades, several explanations have been proposed for the fundamental mechanism of FM. Eaton & Johnston (1982) attributed FM to the unstable balance of mass entrained and released in the separation bubble. Kiya & Sasaki (1983) conjectured that FM reflects the accumulation and emission of vorticity in the separation bubble due to the irregularity of vortex shedding in the separated shear layer, i.e. the 'large vortex'. Driver *et al.* (1987) suspected that FM is caused by the collapse of the separation bubble due to a momentary deficit of engulfment of forward momentum by an irregular vortex shedding, while Tafti & Vanka (1991) explained FM as a gradual build-up and collapse of pressure in the separation bubble. For the turbulent separation induced by a rectangular bluff body of aspect ratio 5, Cimarelli *et al.* (2018) proposed a self-sustained cycle that involves the FM

and small-scale vortex shedding on both sides of the body. This, however, cannot explain the FM observed by Fang *et al.* (2022) beneath a semi-submerged rectangular bluff body, where the shear layer was one-sided. The aforementioned mechanisms of FM all relied on (or were limited to) the dynamics of separated shear layers in a two-dimensional (2-D) plane. Yet Tafti & Vanka (1990, 1991), based on their 2-D and three-dimensional (3-D) simulations of the same separating flow, demonstrated that FM does not occur in 2-D simulation.

The FM is overwhelmed when subjected to excessive incoming turbulence (e.g. Pearson, Goulart & Ganapathisubramani 2013; Fang & Tachie 2020; Fang *et al.* 2021), and is an intrinsic characteristic exclusively for transitional separating flows. It is common in the literature to approximate the transition mechanism of separating flows using the instability originated from the one-dimensional (1-D) reverse-flow profile (see the classical review by Dovgal, Kozlov & Michalke 1994). This simplified instability analysis successively predicts the Kelvin–Helmholtz (KH) instability with sufficient reverse flow (Alam & Sandham 2000; Wee *et al.* 2004) and the receptivity to weak (typically less than 1 % of free-stream velocity) incoming perturbation (Dovgal *et al.* 1994), but demonstrated limited success to describe FM (Yang & Voke 2001; Wee *et al.* 2004). The linear instability analyses for 2-D laminar separating base flows, on the other hand, pronounced the absolutely unstable mode in the form of streamwise elongated streaky structures, instead of the KH instability (Stüer, Gyr & Kinzelbach 1999; Wilhelm, Härtel & Kleiser 2003; Lanzerstorfer & Kuhlmann 2012*a*,*b*). Lanzerstorfer & Kuhlmann (2012*a*,*b*) attributed the absolute instability (or self-sustained) nature of the streaky structures to a combined effect of the lift-up mechanism (Ellingsen & Palm 1975; Landahl 1980; Waleffe 1997; Hwang 2015), feedback influence and flow deceleration (which is measured along the local mean streamlines).

The objective of the present study is to elucidate the kinematic, structural and instability mechanisms underlying FM. To this end, direct numerical simulations are performed for flow separation induced by an infinitely long rectangular plate with a symmetric boundary condition at its centreline. This numerical set-up mimics the experimental condition of Fang *et al.* (2022), and avoids any potential smearing by the unsteadiness originated from the wake flow or shear layer on the opposite side of the plate.

2. Numerical set-up

The momentum conservation for an incompressible Newtonian fluid is governed by

$$\frac{\partial u_i}{\partial t} + u_j \frac{\partial u_i}{\partial x_j} = -\frac{1}{\rho} \frac{\partial p}{\partial x_i} + \nu \frac{\partial^2 u_i}{\partial x_j \, \partial x_j} + F_i, \qquad (2.1)$$

subjected to the constraint $\partial u_i / \partial x_i = 0$. Here, t, p, ρ and ν, respectively, represent time, pressure, density and kinematic viscosity. Velocities in the x_1, x_2 and x_3 (equivalently, x, y and z) directions are denoted by u_1, u_2 and u_3 (equivalently, u, v and w), respectively, while F_i represents generalized forcing in the x_i axis. The spectral element Fourier method by 'Semtex' (Blackburn *et al.* 2019) was used to conduct the present numerical study.

Figure 1 shows the test geometry and employed coordinate system. A sharp-edged bluff body is $20h$, h and $20h$ in the streamwise (x), vertical (y) and spanwise (z) directions, respectively. The leading edge, where the origin of the coordinate system is set, is away from the upstream and top bounds of the computational domain by $25h$ and $20h$, respectively.
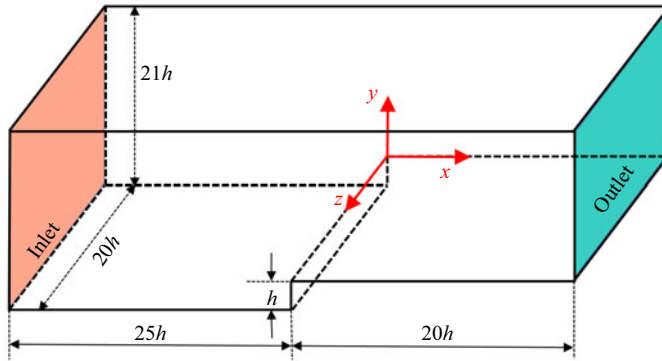
Figure 1. Schematic of the test geometry (not to scale) and employed coordinate system.

A uniform velocity $(u, v, w) = (U_\infty, 0, 0)$ was imposed at the inlet, and the resultant Reynolds number $Re_h \equiv U_\infty h/\nu$ was 2000. The bottom and top planes following the inlet were set to symmetric and free-slip boundary conditions, respectively. The frontal and top surfaces of the bluff body were of the zero-velocity boundary condition. Periodic boundary conditions were applied in the spanwise direction. A narrow ($x/h \in [19.7, 20.0]$) sponge zone was set to use gradually increased forcing (F_i in (2.1)) to bring the velocity to $(u, v, w) = (1.05U_\infty, 0, 0)$ (where 1.05 was to balance the mass flux of inlet) at the outlet for numerical stability. The zero-stress boundary condition was applied at the outlet.

Rectangular spectral elements were used to mesh the x–y plane and clustered over the plate. The smallest side length of the elements (at the leading edge) was $0.036h$, while the height and width of the elements were $0.088h$ and $0.217h$ at $y/h = 2.0$ and $x/h = 20.0$, respectively. In both directions of each element, seventh-order Gauss–Lobatto–Legendre nodes were used. In the spanwise direction, 1024 uniformly distributed grids were used, resulting in a total of 2.2×10^8 independent grids. The grid spacing in all three directions was less than six times the local Kolmogorov length scale. The time step was $0.0008h/U_\infty$, and the Courant–Friedrichs–Lewy number was less than 0.55.

The simulation was initialized using the 2-D laminar solution with random perturbation (Gaussian-distributed white noise) and ran for $250h/U_\infty$ (with several additional rounds of random perturbation over the first $50h/U_\infty$) before reaching statistical equilibrium. After that, the simulation was continued for another $200h/U_\infty$, and 500 samples were collected at a time interval $0.4h/U_\infty$. The above procedure was repeated six times, but with different random perturbations in the process, so as to generate six independent realizations of the same turbulent flow. Approximately three millions core hours were consumed for this study.

3. Results and discussion

As seen in figure 2(*a*), an area of mean flow reversal (see the dashed isopleths) initiates at the leading edge ($x/h = 0$) and terminates at $x/h = 9.05$, which defines the mean reattachment length (L_r). This value of L_r is in good agreement with that ($9.2h$) reported by the experimental study of Fang *et al.* (2022) at a much higher Reynolds number, 14 400. The separation bubble is encompassed by a separated shear layer emanating from the leading edge. This shear layer is visualized conveniently as a cluster of contour levels of U in the figure, and is obviously accompanied with strong magnitudes of $\partial U/\partial y$.
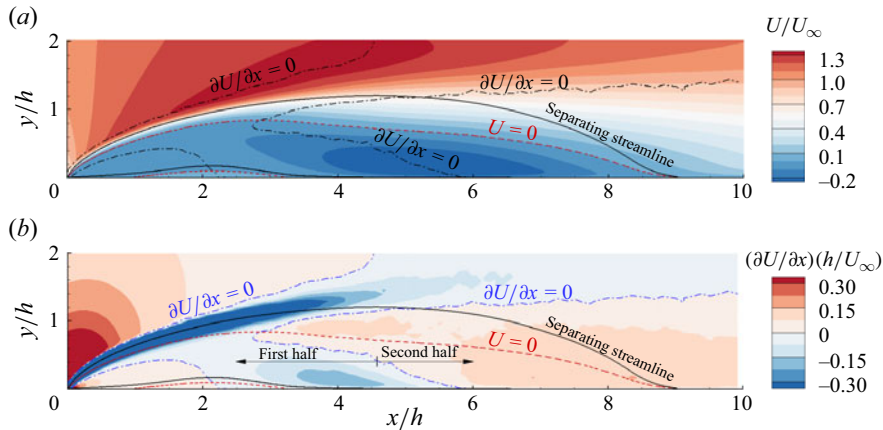
Figure 2. Contours of (*a*) streamwise mean velocity U and (*b*) velocity gradient $\partial U/\partial x$ superimposed with the separating streamline and the isopleths of $U = 0$ and $\partial U/\partial x = 0$. The separating streamline and isopleths of $U = 0$ and $\partial U/\partial x = 0$ are employed for reference in the subsequent plots.

On the other hand, the mean velocity gradient $\partial U/\partial x$ shown in figure 2(*b*) is less obvious than $\partial U/\partial y$ and often overlooked. Strong negatively valued $\partial U/\partial x$ is concentrated along the separated shear layer until the crest of separating streamline. This emphasizes that, other than the mean shear reflected by $\partial U/\partial y$, the separated shear layer also induces significant mean flow deceleration as quantified by $\partial U/\partial x$. This deceleration effect is attributed to the convex curvature of the shear layer, since velocity deficit below the shear layer contributes not only to the shear in the vertical direction, but also to the deceleration in the horizontal direction. It is also interesting to see in figure 2(*b*) that within the separation bubble, the value of $\partial U/\partial x$ switches signs from edges passing through the peak locations of maximum flow reversal. In particular, a local minimum of $\partial U/\partial x$ appears at $x/h \approx 4.0$ near the wall, and is separated from the positively valued $\partial U/\partial x$ at the further downstream location by an inclined edge. This inclined edge well separates the area of flow reversal into two parts, which are termed 'first half' and 'second half' of the separation bubble hereinafter. Since $\partial V/\partial y = -\partial U/\partial x$ holds because of mass conservation and spanwise homogeneity, the distribution of $\partial V/\partial y$ can be deduced easily from figure 2(*b*). For instance, $\partial V/\partial y$ possesses a positive local peak around $x/h = 4.0$ in the first half of the separation bubble.

Figure 3 characterizes a snapshot of low-pass filtered streamwise fluctuating velocity $\widetilde{u'}$ across the separation bubble. For this, a simple spectral filter is employed such that only the frequencies $St_h \equiv fh/U_\infty \leq 0.015$ (the rationale of choosing this threshold will become evident later) are preserved. The maximum root mean square value of streamwise fluctuating velocity (u'_{rms}) is $0.35U_\infty$ (which is also similar to that reported by Fang *et al.* (2022) at a much higher Reynolds number), thus the magnitudes of $\widetilde{u'}$ shown in figure 3 are certainly not weak. In fact, the levels of $\widetilde{u'}$ at $x/h = 1.5$ can become higher than 80 % of the local maximum u'_{rms} in the narrow area flanked by the separating streamline and isopleth of $U = 0$. Furthermore, in the z–y planes at $x/h = 1.5$ and 3.5 (both of which are in the first half of the separation bubble), spanwise elongated positive and negative patches of $\widetilde{u'}$ alternate in the spanwise direction, and $\widetilde{u'}$ switches sign abruptly across the separating streamline in the vertical direction. On the contrary, in the z–y planes at $x/h = 5.5$, 7.5 and 9.5, which are in the second half of the separation bubble, neither the spanwise elongation nor the abrupt sign switching in the vertical direction is discernible.
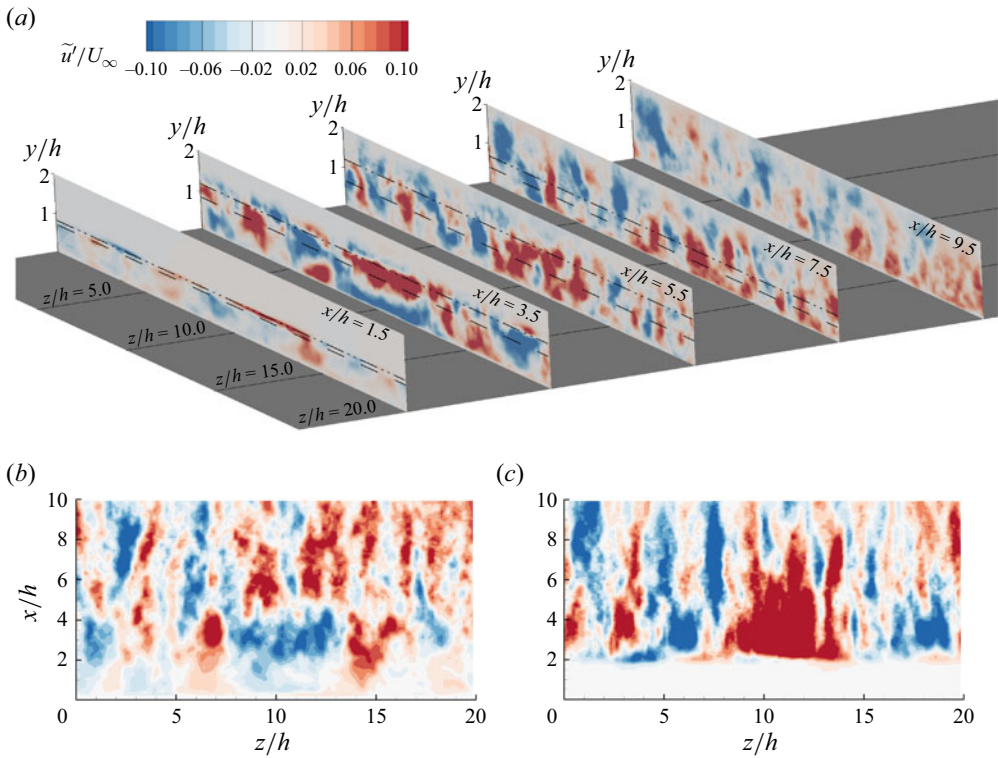
Figure 3. A typical snapshot of the low-pass filtered (retaining only the frequencies $St_h \equiv fh/U_\infty \leq 0.015$) streamwise fluctuating velocity field $\widetilde{u'}$: (*a*) the *z–y* planes at different streamwise locations; (*b,c*) the *z–x* planes at $y/h = 0.3$ and 1.0, respectively. The spanwise dash-dot-dotted and dashed lines in (*a*) mark the elevations of the mean separating streamline and isopleth of $U = 0$, respectively.

Instead, as shown in figures 3(*b,c*), $\widetilde{u'}$ features streamwise elongated streaky structures downstream of $x/h = 4.0$ (i.e. in the second half of the separation bubble). On the other hand, the spanwise vortex shedding triggered by the KH instability (see Cimarelli *et al.* (2018) for an example snapshot) does not manifest at low frequencies. With the above discussion of figure 3, it is now evident that the low-frequency turbulent motion embedded in the flow separation is fundamentally different from the conventional understanding that spanwise vortices originated from the separated shear layer are dominant.

To quantitatively investigate the associated time scales, figure 4 examines the pre-multiplied energy spectrum $\phi_{tke}(f) \equiv \overline{\widehat{u_i}(f)\,\widehat{u_i}^*(f)}$ (where $\overline{(\cdot)}$, $\widehat{(\cdot)}$ and $(\cdot)^*$ denote the ensemble average, Fourier coefficient and complex conjugate, respectively) across the separation bubble. Two branches of frequencies are evident in figure 4(*a*). The high-frequency branch (see the dash-dotted vertical lines) manifests in the shear layer at $x/h \approx 1.5$ with dominant frequency $St_h = 0.70$, and gradually migrates to its subharmonic ($St_h = 0.34$) at $x/h = 5.5$. These observations are attributed to the KH instability and subsequent vortex pairing mechanism in the separated shear layer (Fang *et al.* 2022). The presently observed KH frequency ($St_h = 0.70$) is drastically different from values ($St_h \approx 3$) reported by previous experimental studies at higher Reynolds number (Kiya & Sasaki 1983; Fang *et al.* 2022). The gradual migration of KH frequency to its subharmonic also differs from the discrete migration to multiple subharmonics observed in Fang *et al.* (2022). The above discussion underscores the sensitivity of high-frequency vortical
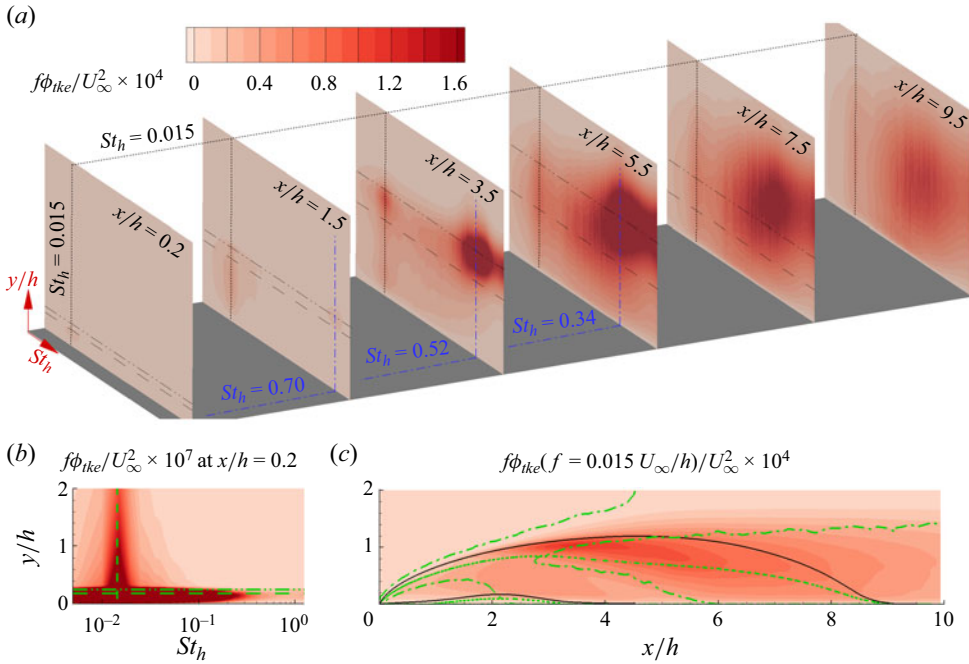
984 A76-6

Figure 4. (*a*) Contours of the pre-multiplied energy spectrum $f\phi_{tke}$ at different streamwise locations. The vertical dashed and dash-dotted lines mark two branches of frequencies. The peaks in the high-frequency branch for $x/h > 5.5$ are indiscernible, and therefore not marked. The dash-dot-dotted and dashed lines along the St_h axis mark the elevations of separating streamline and isopleth of $U = 0$, respectively. The top bound of the plotted y coordinate is $y/h = 2.0$. (*b*) The St_h–y plane at $x/h = 0.2$, but with the contour levels amplified by additional three orders of magnitude. (*c*) The contour of $f\phi_{tke}$ for the frequency $f = 0.015U_\infty/h$ over the entire separation bubble. The same colour bars are used in all plots.

structures to Reynolds number, which is also consistent with the scaling properties of KH frequencies with respect to Reynolds number concluded by Lander *et al.* (2016) and Moore, Letchford & Amitay (2019).

On the other hand, the low-frequency branch in figure 4(*a*) (see the dashed vertical lines) is persistent throughout the entire separation bubble, and its dominant frequency is $St_h = 0.015$, corresponding to $St_{Lr} \equiv fL_r/U_\infty = 0.136$. This value of St_{Lr} is well within $St_{Lr} \in [0.08, 0.2]$ reported for FM in various separated flows/shear layers, regardless of the differences in geometry and Reynolds number (see table 1). As seen in figure 4(*b*), this low-frequency FM is also active in regions away from the separation bubble. It is thus deduced that FM reflects an absolute instability, since its imprint propagates upstream of its origin (Alam & Sandham 2000; Wee *et al.* 2004). This deduction and the streaky structures shown in figure 3 are reminiscent of the absolute unstable mode in the form of streaky structures observed by Lanzerstorfer & Kuhlmann (2012*a*,*b*). Additionally, it is important to note in figure 4(*c*) that the peak energies for the low-frequency branch ($St_h = 0.015$) are concentrated in a narrow area slightly below the crest of the separating streamline.

To isolate the kinematics at different frequencies, the transport equation of the energy spectrum is evaluated, which is derived similarly to Baj & Buxton (2017) and

expressed as

$$
0 = \underbrace{-U_j \frac{\partial \phi_{tke}(f)}{\partial x_j}}_{C(f)} \underbrace{- \frac{1}{\rho} \frac{\partial \mathcal{C}[\hat{p}(f), \widehat{u}_j(f)]}{\partial x_j}}_{D_p(f)} + \underbrace{v \frac{\partial^2 \phi_{tke}(f)}{\partial x_j \, \partial x_j}}_{D_v(f)} \underbrace{- v\mathcal{C}\left[\frac{\partial \widehat{u}_i(f)}{\partial x_j}, \frac{\partial \widehat{u}_i(f)}{\partial x_j} \right]}_{\varepsilon(f)}
$$

$$
\underbrace{- \frac{1}{2} \frac{\partial \mathcal{C}[\widehat{u_i u_j}(f), \widehat{u}_i(f)]}{\partial x_j}}_{D_t(f)} \underbrace{+ \frac{1}{2} \mathcal{C}\left[\widehat{u_i u_j}(f), \frac{\partial \widehat{u}_i(f)}{\partial x_j} \right] - \frac{1}{2} \mathcal{C}\left[\widehat{u_j \frac{\partial u_i}{\partial x_j}}(f), \widehat{u}_i(f) \right]}_{Tr(f)}
$$

$$
\underbrace{- \mathcal{C}[\widehat{u}_i(f), \widehat{u}_j(f)] \frac{\partial U_i}{\partial x_j}}_{Pr(f)} . \tag{3.1}
$$

Here, function $\mathcal{C}[\hat{\xi}(f), \widehat{\varphi}(f)] \equiv \overline{\hat{\xi}(f)\, \widehat{\varphi}^*(f)} + \overline{\hat{\xi}^*(f)\, \widehat{\varphi}(f)}$ defines the co-spectrum of two arbitrary variables ξ and φ (as such, $\int_{-\infty}^{\infty} \mathcal{C}[\hat{\xi}(f), \widehat{\varphi}(f)] \, \mathrm{d}f = \overline{\xi \varphi}$ holds). The terms C, D_p, D_v, ε and D_t quantify the convection, pressure diffusion, viscous diffusion, dissipation and turbulent diffusion, respectively. The Fourier coefficients of nonlinear terms are evaluated as the summation over all combinations of f_1 and f_2 such that $f_1 + f_2 = f$, e.g. $\widehat{u_i u_j}(f) = \sum_{f_1 + f_2 = f} \widehat{u}_i(f_1) \, \widehat{u}_j(f_2)$. The term Tr measures the energy gain/loss by the nonlinear interaction with other pairs of frequencies (namely 'the triadic interaction' as exemplified in Biswas, Cicolin & Buxton 2022), and does not contribute directly to the spatial transport of turbulent kinetic energy ($\frac{1}{2} \overline{u_i' u_i'}$) since $\int_{-\infty}^{\infty} Tr(f) \, \mathrm{d}f \equiv 0$ in theory. The production term (Pr) accounts for the energy extraction from mean flow, and, due to the spanwise homogeneity, possesses four non-zero components as follows:

$$
Pr(f) = \underbrace{-\mathcal{C}[\hat{u}(f), \hat{u}(f)] \frac{\partial U}{\partial x}}_{Pr_{11-n}(f)} \underbrace{- \mathcal{C}[\hat{u}(f), \hat{v}(f)] \frac{\partial U}{\partial y}}_{Pr_{11-s}(f)} \underbrace{- \mathcal{C}[\hat{u}(f), \hat{v}(f)] \frac{\partial V}{\partial x}}_{Pr_{22-s}(f)} \underbrace{- \mathcal{C}[\hat{v}(f), \hat{v}(f)] \frac{\partial V}{\partial y}}_{Pr_{22-n}(f)} .
$$
$$\tag{3.2}$$

Evidently, Pr_{11-s} is dominant for (quasi-)unidirectional shear flows like a zero-pressure-gradient turbulent boundary layer, whereas Pr_{11-n} (by extension Pr_{22-n}, since they are always of opposite signs) is active only in conjunction with significant mean flow acceleration/deceleration.

To pinpoint the generation mechanism of FM, figure 5 examines the budget terms for $\phi_{tke}(f = 0.015 U_\infty/h)$. As seen in the inset of figure 5(a), for the remnants of FM outside the separation bubble (as identified in figure 4b), pressure diffusion (D_p) is the sole constructive mechanism, counterbalanced by the convection (C) and a negative production term Pr_{11-n}. In the reverse flow area for $x/h \leq 1.5$ (see the areas below the horizontal dashed lines in figures 5a,b), convection (C) is the dominant mechanism to energy gain for FM. In contrast, at $x/h = 3.5$ (see figure 5c), there exists substantial energy production by Pr_{11-n} for $y/h \in (0.0, 0.4)$. This production is attributed to the interaction between FM and the mean flow deceleration $\partial U/\partial x$ (see figure 2b) near the wall. It is thus concluded that in the first half of the separation bubble, FM receives energy from the mean flow near $x/h \approx 4.0$ by its streamwise velocity component, then releases energy to the more upstream locations due to the convection by mean flow reversal. In the shear layer of the first half of the separation bubble (near the horizontal dash-dot-dotted lines in
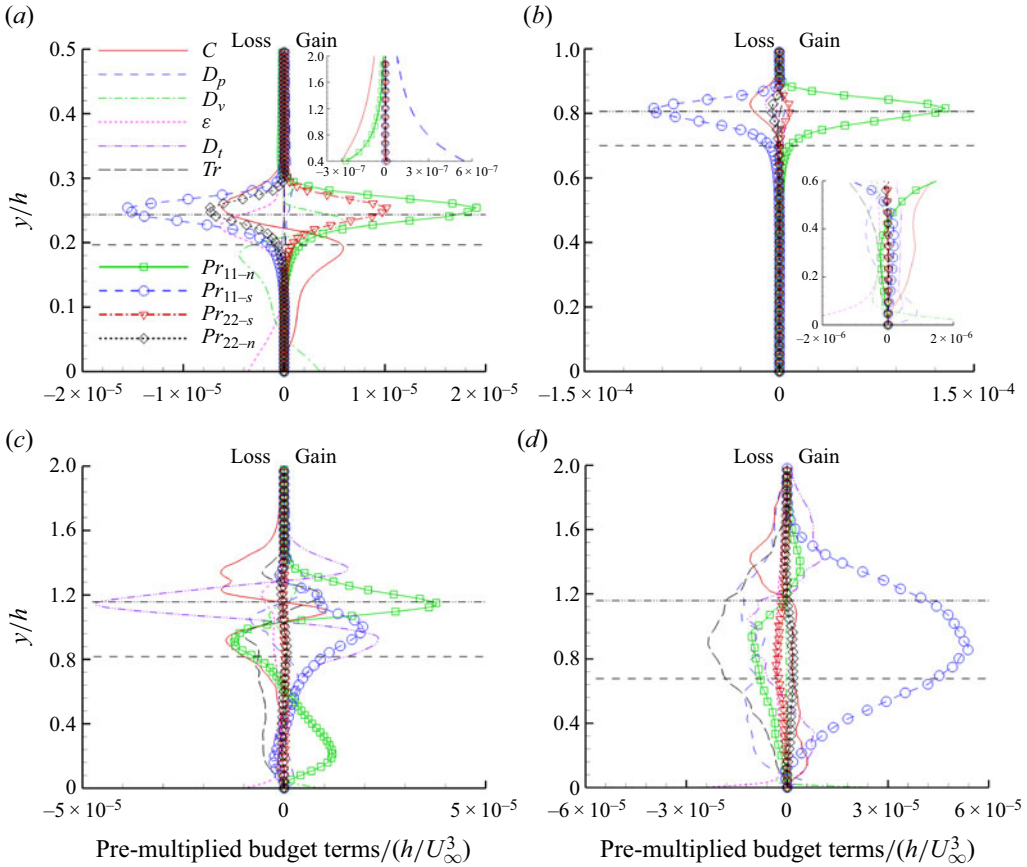
Figure 5. Vertical profiles of budget terms for $\phi_{tke}(f = 0.015U_\infty/h)$ at (*a*) $x/h = 0.2$, (*b*) 1.5, (*c*) 3.5 and (*d*) 5.5. The horizontal dash-dot-dotted and dashed lines mark the elevations of separating streamline and isopleth of $U = 0$, respectively. The insets in (*a*,*b*) magnify the regions above and below the shear layer, respectively.

figures 5*a*–*c*), the dominance of Pr_{11-n} is persistent, signifying a constructive effect of the mean deceleration (i.e. $\partial U/\partial x < 0$) induced by the separated shear layer (see figure 2*b*) on FM. In the second half of the separation bubble (see figure 5*d*), Pr_{11-s} and Tr are the dominant energy source and sink for FM, respectively. This suggests that FM acquires energy from mean flow by the shear $\partial U/\partial y$ of the separated shear layer, before cascading energy towards the high-frequency branch in figure 4. In spite of the drastically different mechanisms of FM in the first and second halves of the separation bubble, it becomes clear now that FM is energized by its interaction with the mean flow (both shear $\partial U/\partial y$ and deceleration $\partial U/\partial x$ shown in figure 2), while its nonlinear interaction with other frequencies is mostly one-way, i.e. damping. Thus the sensitivity of high frequencies to Reynolds number (as commented for figure 4) does not affect FM as much.

To further investigate the structural characteristics of FM, POD is used to decompose the velocity field at frequency $f = 0.015U_\infty/h$ as

$$\hat{\boldsymbol{u}}(x, y, z, f) = \sum_{k=1}^{M} a_f^{(k)}(z) \, \boldsymbol{\Phi}_f^{(k)}(x, y). \tag{3.3}$$
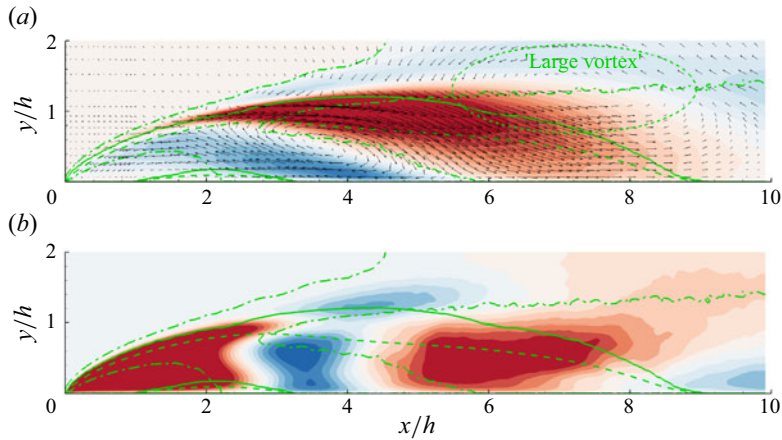
Figure 6. The (*a*) first and (*b*) second POD modes at $St_h = 0.015$ at an arbitrary phase. In (*a*), the contour of streamwise mode velocity is superimposed with the vectors of in-plane mode velocities. In (*b*), the contour is for the spanwise mode velocity. Blue and red are for negative and positive values, respectively. Animated versions are also provided as supplementary movies 1 and 2 available at https://doi.org/10.1017/jfm.2024.280.

Here, $\overline{|a_f^{(k)}|^2}$ measures the energy held by the kth mode at frequency f, while $\boldsymbol{u}_f^{(k)}(x, y, t) \equiv \boldsymbol{\Phi}_f^{(k)}(x, y) \exp(\mathrm{i}2\pi ft) + \mathrm{c.c.}$ (where $\mathrm{i} \equiv \sqrt{-1}$, and c.c. is the complex conjugate counterpart) represents the associated temporally periodic coherent structure, and the associated phase angle is defined as $\alpha \equiv 2\pi ft$. More details of the spectral POD are available in Towne, Schmidt & Colonius (2018) and Fang *et al.* (2022).

Figure 6 shows the first two POD modes at $St_h = 0.015$ (which, respectively, carry 49 % and 13 % of the energy at this frequency). The out-of-plane velocity is zero in the first POD mode, while the in-plane velocities are zero in the second POD modes, reflecting the zero co-spectra between these components (e.g. $\mathcal{C}[\hat{u}(f), \hat{w}(f)]$) due to spanwise homogeneity. The first POD mode features periodic switching between two extreme states of positive and negative streamwise velocity covering the entire separation bubble. The switching between these two states initiates as an abrupt sign switching of streamwise velocity at the crest of the separating streamline, and is followed by a shedding event of a large vortex away from the separation bubble. Both the abrupt sign switching of u' near the crest of separating streamline and the 'large vortex' shedding at the FM frequency have been observed by Kiya & Sasaki (1983) and Tafti & Vanka (1991) for Reynolds numbers $Re_h = 13\,000$ and 500, respectively. The periodic evolution of the first POD mode presented in figure 6(*a*) is the same as that observed by Fang *et al.* (2022) at $Re_h = 14\,400$. With these, it is concluded that FM and its manifestation in the streamwise-vertical plane (by extension, its mechanism) are insensitive to Reynolds number.

As seen in figure 6(*b*), the spanwise mode velocity goes in and out of the plane in transient areas, and the boundaries where it switches signs can be interpreted as vortex filaments passing the plane. In the first half of the separation bubble, two vortex filaments (see the white bands at $x/h \approx 3$ and 4 in the figure) occasionally emerge and are both nearly in the vertical direction. As time evolves, the upstream vortex moves towards the leading edge quickly, whereas the downstream one is 'reluctant' to leave $x/h \approx 4$ before eventually being displaced. Indeed, the positive $\partial V/\partial y$ (as deduced from figure 2*b*) stretches, and consequently amplifies, the vertical vortex in the first half of the separation bubble near the wall. Further, the aforementioned vortex initiating at $x/h = 4$ on the

wall abruptly changes orientation from vertical to horizontal at the highest point of the separating streamline. This is attributed to the generation of streamwise vorticity by tilting the vertical vorticity through shear, i.e. $\omega_2' \, \partial U/\partial y$, where $\omega_2' \equiv (\partial u'/\partial z - \partial w'/\partial x)$ is the vertical vorticity. It is also noted in figure 6(*b*) (and its animation) that the vortices in the second half of the separation bubble exhibit a strong tendency of aligning in the streamwise direction. This signifies the vortex stretching by mean flow acceleration (see the positive $\partial U/\partial x$ in figure 2(*b*) in the area).

The topological characteristics of the 3-D structure associated with FM can be determined using the correlation function $\hat{\boldsymbol{u}}_{FM} \equiv \overline{\hat{\boldsymbol{u}}(x, y, z_{ref} + \Delta z, f) \, a_f^{(1)}(z_{ref})}$, where f is set to $0.015U_\infty/h$, and z_{ref} denotes a chosen reference z plane, in the spirit of linear stochastic estimation (Adrian & Moin 1988). Figure 7 characterizes the evolving features of FM in 3-D space using $u_{FM} \equiv \hat{u}_{FM} \exp(i\alpha) +$ c.c. From figures 7(*a,c,e*), the streamwise elongated streaky structures are persistent especially downstream of $x/h = 4$, similar to the low-pass filtered velocity shown in figure 3. The low- and high-velocity streaky structures alternate in the spanwise direction and vary with phase (time). The low-velocity streak in figure 7(*a*) in the region $x/h > 4$ possesses spanwise width $7h$, and separates from the spanwise adjacent high-velocity streak by a vertical vortex near $x/h = 4$. This low-velocity streak, as shown in figure 7(*b*), covers almost the entire separation bubble over its spanwise width. As the phase (α) evolves to that in figures 7(*c,d*), this low-velocity streak becomes narrower in the spanwise direction, and opposite-signed smaller vertical vortices, flanking a small spot of positive u', emerge at its spanwise centre in the immediate vicinity of $x/h = 4$. Meanwhile, further downstream of $x/h = 4$, the values of u' in the centre of the low-velocity streak increase over its entire vertical thickness. Subsequently, as shown in figures 7(*e,f*), the low-velocity streak gradually shrinks in size, and its remnant before complete disappearance is noticeable upstream of $x/h = 4$ while maintaining its spanwise width ($\approx 3.2h$). Downstream of $x/h = 4$, on the other hand, a new low-velocity streak manifests and is offset from the spanwise centre of the previous low-velocity streak by $4.8h$. This spanwise offset is the same as that for the high-velocity streak observed in figure 7(*a*). This implies that the isosurface of $u_{FM} = -0.15 \, |\hat{u}_{FM}|_{max}$ in figure 7(*f*) is similar to the isosurface of $u_{FM} = 0.15 \, |\hat{u}_{FM}|_{max}$ (note the sign) in figure 7(*b*). Therefore, the above evolution process and the counterpart opposite-signed version form the cycle of 3-D structures associated with FM. This 3-D nature of FM is in direct contrast to the previously conjectured generation mechanisms of FM without resorting structures in 3-D space (Eaton & Johnston 1982; Kiya & Sasaki 1983; Driver *et al.* 1987; Cimarelli *et al.* 2018), and also explains why FM does not occur in the 2-D simulation of Tafti & Vanka (1990) but did occur in the counterpart 3-D simulation of Tafti & Vanka (1991).

A conceptual vortex model evolving in 3-D space is proposed in figure 8 to incorporate all aforementioned kinematic and structural characteristics of FM, as well as those gleaned from the literature. When the low-velocity streak covers the separation bubble (as in figures 7*a,b*), the separated shear layer is elevated and flow reattachment is delayed. This accounts for the state of an enlarged separation bubble at a low frequency reported in the literature (e.g. Eaton & Johnston 1982; Kiya & Sasaki 1983; Fang *et al.* 2022). This enlarged separation bubble in the x–y plane, as shown in figures 8(*a,b*), is flanked by vertical (marked as VA) and streamwise (marked as SA) vortices in the first and second halves of the separation bubble, respectively, from a 3-D perspective. (Note that the mirrored versions of the vortices, such as VA′, are not explicitly commented on hereinafter for conciseness in the text.) The dominance of vertical vortices in the first half of the separation bubble has been shown in figure 6(*b*). The vertical vorticity (ω_2') generated by
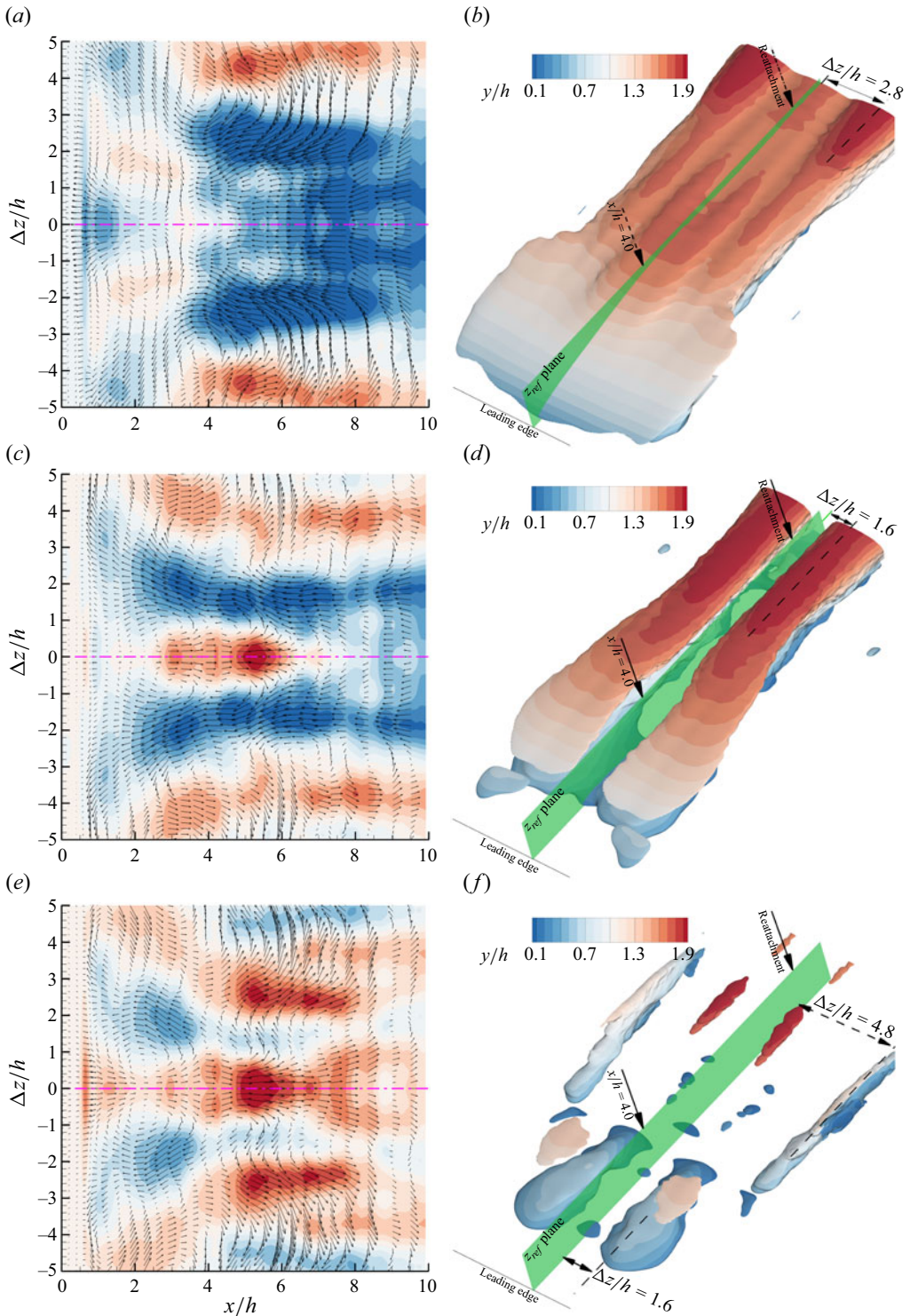
Figure 7. (*a,c,e*) Contours of u_{FM} superimposed with the associated in-plane velocity vectors at $y/h = 0.5$. (*b,d,f*) The isosurfaces of $u_{FM} = -0.15\,|\hat{u}_{FM}|_{max}$ for the phase angles (*a,b*) $\alpha = -\pi/6$, (*c,d*) $\alpha = 0$ and (*e,f*) $\alpha = \pi/9$, coloured by the vertical elevation (y/h). An animated version of (*a,c,e*) is also provided as supplementary movie 3.
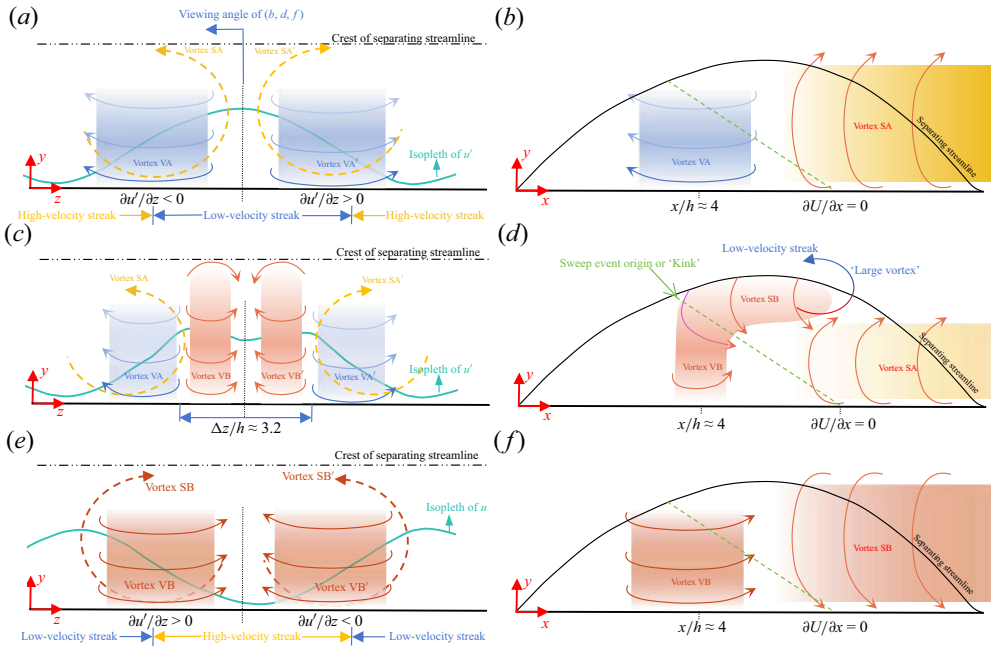
Figure 8. A conceptual vortex model (not to scale) viewed from the (*a,c,e*) upstream and (*b,d,f*) side locations for the same phase angles as in figure 7. Notations VA , VB, SA, SB′ and so on are used to denote pertinent vortices. Here, the first letter (V or S) distinguishes the vertical and streamwise vortices, and the second letter (A or B) is for enumeration, whereas the superscript prime denotes a mirrored version. Note in (*d*) that vortex SA is further back into the viewing plane than vortices VB and SB, and vortex VA behind VB is omitted for clarity.

$\partial u'/\partial z$ near the boundaries segregating the low- and high-velocity streaks in the spanwise direction is prone to stretching by positive $\partial V/\partial y$ (especially in the near-wall region around $x/h = 4.0$; see figure 2*b*), and is therefore sustained in the first half of the separation bubble. The streamwise vortices in the second half of the separation, on the other hand, are stretched and sustained by the mean flow acceleration $\partial U/\partial x$ (see figure 2*b*), and their origin of generation is explained as follows.

As the phase evolution continuous to that in figures 8(*c,d*) (or equivalently, figures 7*c,d*), the vortices VA and SA induce two interconnected pairs of opposite-signed vortices (marked as VB and SB). The vertical vortex VB is centred in the vicinity of $x/h = 4$ to be amplified by the local vertical stretching. The streamwise vortex SA, on the other hand, is near the crest of the separating streamline. The interconnection of the vertical vortex VB and streamwise vortex SB in figure 8(*d*) reflects a mutual induction mechanism and an absolute instability mechanism.

Let us elaborate this mutual induction mechanism first. Near the crest of the separating streamline, the mean shear $\partial U/\partial y$ tilts streamwise vorticity to form vertical vorticity, and vice versa. This tilting effect is abrupt and creates a strong curvature at the crest of the separating streamline. The point where the vortices switch orientation is termed a 'kink', following Zhou *et al.* (1999). Based on the discussion of the Biot–Savart law for hairpin structures by Zhou *et al.* (1999), the strong curvature near the kink significantly enhances the velocity induction in the space flanked by counter-rotating vortices. Indeed, in the corner of VB and SB, the spanwise velocity w' induced by SB can also drive VB,

and vice versa, i.e. mutual induction. This mutual induction, along with the stretching by $\partial V/\partial y$ and $\partial U/\partial x$, strengthens VB and SB in the first and second halves of the separation bubble, respectively. Because of this process, the sweep event initiates near the crest of the separating streamline, and then spills over the entire separation bubble. Meanwhile, the low-velocity streak in the region above the separating streamline is altered only mildly. This, together with the sweep event underneath the separating streamline, weakens the instantaneous shear layer, while generating a 'large vortex'. This 'large vortex' gradually deviates from its original position while decaying, and, in the process, introduces (albeit weak) disturbance outside the separation bubble. This 'large vortex' has been reported as a feature of FM (see also figure 6(*a*) here), and conjectured to be some irregularity of vortex shedding in the separated shear layer in the literature (e.g. Kiya & Sasaki 1983; Tafti & Vanka 1991; Yang & Voke 2001). With the above discussion, it is now clear that in fact this 'large vortex' is not due to the irregularity of vortex shedding, but is a consequence of abrupt switching between low- and high-velocity streaky structures due to the evolution of vortices initiated at the crest of the separating streamline.

Let us now comment on the instability mechanism sustaining FM. To this end, a negative v' near the crest of the separating streamline, as that induced by SB in figures 8(*c*,*d*), is considered. Since $V \approx 0$ for obvious reasons, an infinitesimal u' is governed approximately by

$$\frac{\partial u'}{\partial t} + v' \frac{\partial U}{\partial y} + u' \frac{\partial U}{\partial x} + U \frac{\partial u'}{\partial x} \approx 0. \tag{3.4}$$

Similar to the framework of Prandtl's mixing length hypothesis, the negative v' in the separated shear layer generates positive u' (i.e. a sweep event, as marked in figure 8*d*), thus the second term of (3.4) is negative. With the negative $\partial U/\partial x$ near the crest of the separating streamline (see figure 2*b*), the third term of (3.4) is also negative. Because of the streamwise orientation of SB, $\partial u'/\partial x \approx 0$ holds, especially at the location of maximum u', so that the fourth term of (3.4) is relatively negligible. It is therefore concluded that for the sweep event induced by SB near the crest of separating streamline, $\partial u'/\partial t$ is positive to further amplify the already-positive u', i.e. instability. This instability is similar to the lift-up mechanism, which is described by (3.4) without the third and fourth terms as in Ellingsen & Palm (1975). The third term of (3.4), due to the mean flow deceleration ($\partial U/\partial x < 0$) near the crest of separating streamline, provides an additional boost to the lift-up mechanism. This 'boosted' lift-up mechanism explains the elevated productions due to shear ($Pr_{11,s}$) and deceleration ($Pr_{11,n}$) for FM at the crest of the separating streamline (see figure 5*c*). This is also why the elevated levels of energy of FM (figure 4*c*) and the abrupt appearance of a sweep (or ejection) event (see the animation for figure 6*a*) are both near the crest of the separating streamline. This boosted lift-up mechanism is reminiscent of the absolute instability of streaky structures observed by Lanzerstorfer & Kuhlmann (2012*a*,*b*). This boosted lift-up mechanism cannot be captured by the instability analyses based on 1-D reverse-flow profiles (i.e. omitting the streamwise variation of base flow), which have demonstrated limited success in describing FM (e.g. Yang & Voke 2001).

As the vortices VB and SB in figures 8(*c*,*d*) evolve to those in figures 8(*e*,*f*), the sweep event gradually covers the entire separation bubble, resulting in a high-velocity streak in the original location of the low-velocity streak. During this process, the vortex cores of VB and SB gradually deviate from the separated shear layer, so that the mutual induction becomes inactive. This breaks the connection between VB and SB to be as in figures 8(*e*,*f*). Subsequently, VB and SB in figures 8(*e*,*f*) act as opposite-signed versions of vortices VA and SA in figures 8(*a*,*b*), and this cycle repeats.

4. Conclusions

The fundamental mechanism of low-frequency flapping motion (FM) in flow separation is investigated using direct numerical simulation. In the mean flow reversal area, streamwise deceleration and acceleration (together with positive and negative $\partial V/\partial y$, respectively) manifest in the first and second halves of the separation bubble, respectively. The separated shear layer, on the other hand, features not only the vertical shear (i.e. positive $\partial U/\partial y$) but also streamwise deceleration (i.e. negative $\partial U/\partial x$). Near the crest of the separating streamline, the lift-up mechanism due to shear is boosted by deceleration, and triggers the instability underlying FM. In the meantime, the shear abruptly tilts the streamwise vorticity to vertical vorticity (and vice versa), creating a strong curvature in the vortex filament. For this vortex filament, the vertical part is stretched by the positive $\partial V/\partial y$ in the first half of the separation bubble, and the streamwise part is stretched by the positive $\partial U/\partial x$ in the second half of the separation bubble. The vertical and streamwise parts of the vortex filament can also self-sustain by a mutual induction mechanism, and collaboratively create low-velocity (or high-velocity) streaky structures encompassing the entire separation bubble, so as to flap the separated shear layer up and down periodically. A 'large vortex' shedding manifests at the interface between the low- and high-velocity streaks during the sign switching, and introduces perturbation outside the separation bubble. This 'large vortex' is not the previously conjectured irregularity of vortex shedding residing in the separated shear layer in the literature. Overall, FM is unstable, self-sustained, and manifests outside the separation bubble, and therefore represents an absolute (global) instability.

The frequency f of FM, when scaled by the mean reattachment length L_r and free-stream velocity U_∞, is well known to be within a narrow band $St_{Lr} \equiv fL_r/U_\infty \in [0.08, 0.20]$, regardless of geometry, pressure gradient or Reynolds number. This hints at the universality of FM. As has been elucidated, FM is triggered by a boosted lift-up mechanism at the crest of the separating streamline, which relies on the co-existence of shear (positive $\partial U/\partial y$) and deceleration (negative $\partial U/\partial x$). This co-existence of shear and deceleration is expected to be universal for separated shear layers since they are always convex. The evolution of FM also involves the positive $\partial V/\partial y$ (equivalently, negative $\partial U/\partial x$) and positive $\partial U/\partial x$ in the first and second halves of the separation bubble, respectively. The negative and positive values of $\partial U/\partial x$ are separated naturally in space by the maximum reverse flow at the centre of any separation bubbles. The topological distribution of these mean (or base) flow properties supporting FM is thus universal, and the mean reattachment length L_r is indeed an appropriate length scale for FM. Therefore, the universality of FM is suggested.

Author ORCIDs.
Xingjun Fang https://orcid.org/0000-0003-2005-7269;
Zhan Wang https://orcid.org/0000-0003-4393-2118.

REFERENCES

ADRIAN, R.J. & MOIN, P. 1988 Stochastic estimation of organized turbulent structure: homogeneous shear flow. *J. Fluid Mech.* **190**, 531–559.

ALAM, M. & SANDHAM, N.D. 2000 Direct numerical simulation of 'short' laminar separation bubbles with turbulent reattachment. *J. Fluid Mech.* **410**, 1–28.

BAJ, P. & BUXTON, O.R.H. 2017 Interscale energy transfer in the merger of wakes of a multiscale array of rectangular cylinders. *Phys. Rev. Fluids* **2**, 114607.

BISWAS, N., CICOLIN, M.M. & BUXTON, O.R.H. 2022 Energy exchanges in the flow past a cylinder with a leeward control rod. *J. Fluid Mech.* **941**, A36.

BLACKBURN, H.M., LEE, D., ALBRECHT, T. & SINGH, J. 2019 Semtex: a spectral element–Fourier solver for the incompressible Navier–Stokes equations in cylindrical or Cartesian coordinates. *Comput. Phys. Commun.* **245**, 106804.

CHERRY, N.J., HILLIER, R. & LATOUR, M.E.M.P. 1984 Unsteady measurements in a separated and reattaching flow. *J. Fluid Mech.* **144**, 13–46.

CHIATTO, M., DE LUCA, L., HLEVCA, D. & GRASSO, F. 2021 Modal analysis of actively controlled flow past a backward facing ramp. *Phys. Rev. Fluids* **6**, 064608.

CIMARELLI, A., LEONFORTE, A. & DE ANGELI, E. 2018 On the structure of the self-sustaining cycle in separating and reattaching flows. *J. Fluid Mech.* **857**, 907–936.

DOVGAL, A.V., KOZLOV, V.V. & MICHALKE, A. 1994 Laminar boundary layer separation: instability and associated phenomena. *Prog. Aerosp. Sci.* **30**, 61–94.

DRIVER, D.M., SEEGMILLER, H.L. & MARVIN, J.G. 1987 Time-dependent behavior of a reattaching shear layer. *AIAA J.* **25** (7), 914–919.

EATON, J.K. & JOHNSTON, J.P. 1982 Low frequency unsteadiness of a reattaching turbulent shear layer. *Turbul. Shear Flows* **3**, 162–170.

ELLINGSEN, T. & PALM, E. 1975 Stability of linear flow. *Phys. Fluids* **18**, 487–488.

FANG, X. & TACHIE, M.F. 2020 Spatio-temporal dynamics of flow separation induced by a forward-facing step submerged in a thick turbulent boundary layer. *J. Fluid Mech.* **892**, A40.

FANG, X., TACHIE, M.F., BERGSTROM, D.J., YANG, Z. & WANG, B.C. 2021 Three-dimensional structural characteristics of flow separation induced by a forward-facing step in a turbulent channel flow. *J. Fluid Mech.* **919**, A24.

FANG, X., TACHIE, M.F. & DOW, K. 2022 Turbulent separations beneath semi-submerged bluff bodies with smooth and rough undersurfaces. *J. Fluid Mech.* **947**, A19.

FRICKE, F.R. 1971 Pressure fluctuations in separated flows. *J. Sound Vib.* **17** (1), 115–123.

HUDY, L.M., NAGUIB, A.M. & HUMPHREYS, W.M. 2003 Wall-pressure-array measurements beneath a separating/reattaching flow region. *Phys. Fluids* **15** (3), 706–717.

HWANG, J. 2015 Statistical structure of self-sustaining attached eddies in turbulent channel flow. *J. Fluid Mech.* **767**, 254–289.

KIYA, M. & SASAKI, K. 1983 Structure of a turbulent separation bubble. *J. Fluid Mech.* **137**, 83–113.

KIYA, M., SASAKI, K. & ARIE, M. 1982 Discrete-vortex simulation of a turbulent separation bubble. *J. Fluid Mech.* **120**, 219–244.

LANDAHL, M.T. 1980 A note on an algebraic instability of inviscid parallel shear flows. *J. Fluid Mech.* **98** (2), 243–251.

LANDER, D.C., LETCHFORD, C.W., AMITAY, M. & KOPP, G.A. 2016 Influence of the bluff body shear layers on the wake of a square prism in a turbulent flow. *Phys. Rev. Fluids* **1**, 044406.

LANZERSTORFER, D. & KUHLMANN, H.C. 2012*a* Global stability of the two-dimensional flow over a backward-facing step. *J. Fluid Mech.* **693**, 1–27.

LANZERSTORFER, D. & KUHLMANN, H.C. 2012*b* Three-dimensional instability of the flow over a forward-facing step. *J. Fluid Mech.* **695**, 390–404.

LARGEAU, J.F. & MORINIERE, V. 2007 Wall pressure fluctuations and topology in separated flows over a forward-facing step. *Exp. Fluids* **42**, 21–40.

MOHAMMED-TAIFOUR, A. & WEISS, J. 2016 Unsteadiness in a large turbulent separation bubble. *J. Fluid Mech.* **799**, 383–412.

MOORE, D.W., LETCHFORD, C.W. & AMITAY, M. 2019 Energetic scales in a bluff body shear layer. *J. Fluid Mech.* **875**, 543–575.

PASSAGGIA, P.-Y., LEWEKE, T. & EHRENSTEIN, U. 2012 Transverse instability and low-frequency flapping in incompressible separated boundary layer flows: an experimental study. *J. Fluid Mech.* **703**, 363–373.

PEARSON, D.S., GOULART, P.J. & GANAPATHISUBRAMANI, B. 2013 Turbulent separation upstream of a forward-facing step. *J. Fluid Mech.* **724**, 284–304.

SPAZZINI, P.G., IUSO, G., ONORATO, M., ZURLO, N. & DI CICCA, G.M. 2001 Unsteady behavior of back-facing step flow. *Exp. Fluids* **30** (5), 551–561.

STÜER, H., GYR, A. & KINZELBACH, W. 1999 Laminar separation on a forward facing step. *Eur. J. Mech. B/Fluids* **18**, 675–692.

TAFTI, D.K. & VANKA, S.P. 1990 A numerical study of the effects of spanwise rotation on turbulent channel flow. *Phys. Fluids* A **3** (4), 642–656.

TAFTI, D.K. & VANKA, S.P. 1991 A three-dimensional numerical study of flow separation and reattachment on a blunt plate. *Phys. Fluids* A **3**, 2887–2909.

THACKER, A., AUBRUN, S., LEROY, A. & DEVINANT, P. 2013 Experimental characterization of flow unsteadiness in the centerline plane of an Ahmed body rear slant. *Exp. Fluids* **54**, 1479.

TOWNE, A., SCHMIDT, O.T. & COLONIUS, T. 2018 Spectral proper orthogonal decomposition and its relationship to dynamic mode decomposition and resolvent analysis. *J. Fluid Mech.* **847**, 821–867.

WALEFFE, F. 1997 On a self-sustaining process in shear flows. *Phys. Fluids* **9** (4), 883–900.

WEE, D., YI, T., ANNASWAMY, A. & GHONIEM, A.F. 2004 Self-sustained oscillations and vortex shedding in backward-facing step flows: simulation and linear instability analysis. *Phys. Fluids* **16** (9), 3361–3373.

WILHELM, D., HÄRTEL, C. & KLEISER, L. 2003 Computational analysis of the two-dimensional-three-dimensional transition in forward-facing step flow. *J. Fluid Mech.* **489**, 1–27.

YANG, Z. & VOKE, P.R. 2001 Large-eddy simulation of boundary-layer separation and transition at a change of surface curvature. *J. Fluid Mech.* **439**, 305–333.

ZHOU, J., ADRIAN, R.J., BALACHANDAR, S. & KENDALL, T.M. 1999 Mechanisms for generating coherent packets of hairpin vortices in channel flow. *J. Fluid Mech.* **387**, 353–396.